Energy Conversion and Management 156 (2018) 10–24

Contents lists available at ScienceDirect

Energy Conversion and Management

journal homepage: www.elsevier.com/locate/enconman

An efficient temperature swing adsorption (TSA) process for separating CO_2 from CO_2/N_2 mixture using Mg-MOF-74

Rached Ben-Mansour*, Naef A.A. Qasem

Mechanical Engineering Department and KACST-TIC on CCS, King Fahd University of Petroleum & Minerals, Dhahran 31261, Saudi Arabia

ARTICLE INFO

Keywords:
Carbon capture
Adsorption
Carbon-dioxide
Separation
TSA
CFD
Mg-MOF-74

ABSTRACT

Carbon dioxide emitted from fossil fuel burning processes is quantitatively the most contributor to global warming. It is believed that climate change could be mitigated by means of Carbon Capture and Storage (CCS). CO_2 physical adsorption separation has the potential of capture carbon dioxide with minimum energy costs. A special type of metal organic frameworks named Mg-MOF-74 is an exceptional adsorbent amongst other porous materials with high CO_2 uptake at flue gas conditions. Temperature swing adsorption (TSA) composed of 4 steps (feed, rinse, heating, and cooling), for separating CO_2 from CO_2/N_2 mixture using Mg-MOF-74; has been mathematically modeled. A computer model implementation was developed employing User-Defined-Functions linked to Ansys-Fluent software. The CFD two- and three-dimensional models have been validated against adsorption breakthrough experimental data obtained by the authors, at ambient temperature, and against published experimental data for high temperature conditions.

The regeneration (heating and cooling) time has been tuned to explore the performance improvement for the TSA process. The TSA optimal key performance indices in terms of CO_2 purity, recovery, productivity, and process power consumption have been found to be 96.22%, 86.5%, 0.279 kg of CO_2 per hour per kg of Mg-MOF-74, and 663.8 kWh per ton of CO_2 captured, respectively. These productivity and power consumption values showed a substantial enhancement in the CO_2 adsorption separation compared to those reported in the literature, especially when the heating process is used for the desorption part of the process.

1. Introduction

The greenhouse gases emitted from combustion processes contain carbon dioxide, water vapor, nitrogen oxide and methane. It is believed by the majority of atmospheric scientists that global warming caused by these gases can lead to atmospheric heat waves, shore floods, land droughts, destruction of cold-marine life and whole ecosystems as well as the economic difficulties that may result in a reduction of the world's gross domestic product by 5–20% [1]. The relative increase of the world temperature was about 0.74% in last 100 years and is expected to reach 6.4% at the end of this century [1]. Large amounts of glaciers ice have been melting causing at least 0.2 mm/year rise in global sea level [2]. The most predominant of the greenhouse gases is carbon dioxide [3]. Fossil fuel is the prevailing source of the global primary energy demand, and will continue to be so during the next few decades. Since CO_2 is considered the main promoter for climate change, carbon capture (CC) is an essential solution to keep using fossil fuels while minimizing the emissions of CO_2 into the atmosphere, and thereby mitigating global climate change. Research is the only way to address technical challenges of carbon capture such as improved efficiency and reduced cost of CO_2 capture [4].

Many researchers have studied CO_2 separation and storage, using both experimental and simulation methods as well as developing novel adsorbents for this purpose [5]. The impact of adsorbent thermophysical properties on CCS are also reviewed [6]. The utmost merit of using adsorption for CO_2 separation is the ease of regeneration of the adsorbent material by applying heat and/or vacuum [7]. Activated carbon and zeolite are the most common known adsorbents being utilized for CO_2 separation and storage. Zeolites could be used more than activated carbon for CO_2 capture and hydrogen storage in low pressure applications [8,9], whereas activated carbon materials have been desired for high pressure processes [9,10]. However, the obvious merits of activated carbon materials over zeolites include cost-effectiveness, hydro-stability, lower energy required for regeneration due to lower heat of adsorption [11]. Alkaline paper mill waste (APMW) could also be used to separate CO_2 from coal-fired power plants [12]. Carbon capture, along with hydrogen production were also proposed [13,14]. Recently, a novel class of porous materials has been synthesized and

* Corresponding author.
E-mail address: rmansour@kfupm.edu.sa (R. Ben-Mansour).

https://doi.org/10.1016/j.enconman.2017.11.010
Received 6 July 2017; Received in revised form 2 November 2017; Accepted 3 November 2017
Available online 08 November 2017
0196-8904/ © 2017 Elsevier Ltd. All rights reserved.

Nomenclature

C	concentration, mol m^{-3}
C_p	specific heat capacity, J kg^{-1} K^{-1}
D, d	diameter, size, m
D_{disp}	mass dispersion coefficient, m^2 s
E_g	total gas energy, J m^{-3}
E_s	total adsorbent energy, J m^{-3}
h	sensible enthalpy, J kg^{-1}
h_{ext}	external heat transfer confident, W m^{-2} K^{-1}
h_{int}	internal heat transfer coefficient, W m^2 K^{-1}
ΔH	heat of adsorption, J mol^{-1}
$\vec{g}$	gravity acceleration vector, m s^{-2}
$\vec{J}$	Diffusion flux, kg m^{-2} s^{-1}
K_o	Toth adsorption constants, Pa^{-1}
K_{eq}	isotherm adsorption constant, Pa^{-1}
k	thermal conductivity, W m^{-1} K^{-1}
k_L	LDF adsorption time constant, s^{-1}
M	molecular weight, kg mol^{-1}
n	isotherms adsorption constant
q	adsorption uptake, mmol g^{-1}
q^*	equilibrium adsorption uptake, mmol g^{-1}
q_m	adsorption uptake limit, mmol g^{-1}
Q_F	feed volumetric flow rate at standard conditions, m^3 s^{-1}
P	pressure, Pa
R	universal gas constant, J mol^{-1} K^{-1}
r	radius, m
Re	Reynolds number
t	time, s
T	temperature, K
tss	Stoichiometric time, s
$\bar{\bar{\tau}}$	stress sensor, N m^{-2}
x	mole fraction
y	mass fraction
$\vec{v}$	velocity vector, m s^{-1}

Greek letters

ρ	mixture gas density, kg m^{-3}
ε	bed porosity
ε	thermal emissivity
μ	dynamic viscosity, Pa s^{-1}
σ	Steffen Boltzmann coefficient, W m^{-2} K^{-4}
τ	tortuosity

Subscript

eff	effective
p	particle
pore	adsorbent pore
i	gas species index
g	gas
s	standard conditions
0	inlet, saturation
w	wall

called metal-organic frameworks (MOFs) [15]. MOF-74 is the most currently available MOFs with high CO_2 adsorption capacity as well as an excellent CO_2 over N_2 selectivity [16,17]. More specifically, Mg-MOF-74 was quantitatively identified as the highest adsorbent adsorbs CO_2 at low-pressure conditions (350 mg/g at 298 K and l bar); the shape of Mg-MOF-74 was virgin powder. [17].

A considerable number of experimental and numerical research attempts based on CO_2 capture and separation have been conducted so far in terms of breakthrough and pressure and temperature swing adsorption [18–34]. Experimental and numerical investigations of CO_2

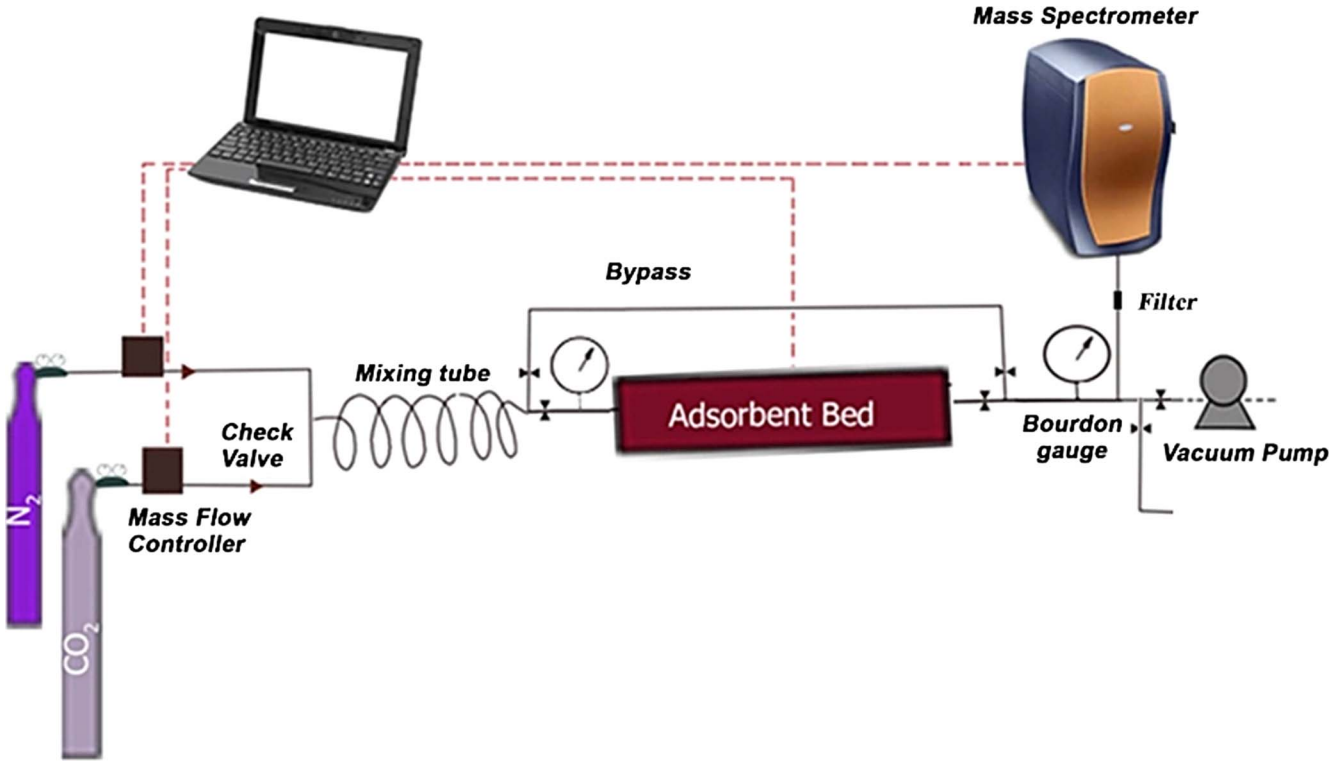

Fig. 1. Schematic diagram of carbon dioxide adsorption capture breakthrough setup.

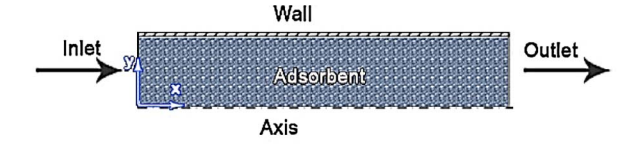

(a) 2D Adsorbent bed.

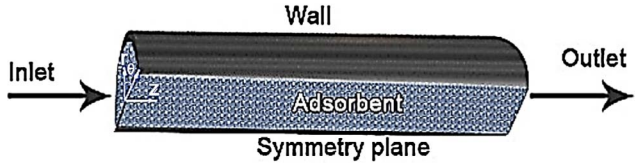

(b) 3D adsorbent bed.

Fig. 2. Adsorbent beds used for CO_2 separation.

removal from flue gas using natural and synthetic zeolites indicated that synthetic zeolites (such as 5A and 13X) are most encouraging adsorbents for CO_2 capture from combustion products [35–38]. Zeolite 13X-APG was used for CO_2 separation by experimental vacuum pressure swing adsorption technique by Wang et al. [32]. The results showed that CO_2 recovery and purity were about 85–95% and 37–82%, respectively, with power consumption about 1.79–2.14 MJ $kg_CO_2^{-1}$ and CO_2 productivity about 0.207 $mol_CO_2\ m^{-3}$ of adsorbent. Zeolite 13X-APG was also utilized [31] for post combustion CO_2 capture by VTSA process. The study concentrated mainly on the type of regeneration process such as TSA, VSA and VTSA that had more CO_2 recovery and purity. The comparison of results among the three regeneration methods (TSA, VSA and VTSA) illustrated that the best CO_2 recovery and purity of VSA process were 78.6% and 78.4%, respectively, at P = 3 kPa for 5 min of evacuation and 0.15 SLPM of N_2 purging. TSA process without evacuation could achieve 78.1% of CO_2 recovery and 91.6% of CO_2 purity for 443 K of desorption. The cooling was carried out close to ambient conditions during 10 min to raise adsorption uptake. Conversely, vacuum temperature swing adsorption (VTSA) at 403 K and 3 kPa could achieve 98.2% and 94% of CO_2 recovery and purity, respectively.

The research conducted by the literature showed that the performance of physical swing adsorption processes using traditional adsorbents (such as activated carbon and zeolite) is still not commercially attractive and needs some improvements. Mg-MOF-74 was shown as the best adsorbent reported for CO_2 separation at flue gas conditions. Moreover, multidimensional CFD modeling for CO_2 swing adsorption was not presented well. Therefore, this work aims at 2D/3D temperature swing adsorption modeling for CO_2 separation from binary mixture (CO_2/N_2) using Mg-MOF-74. The advantages of using 2D/3D adsorption models are explained next. Including two- or three-dimensional models can lead to accurate heat and mass transfer and adsorption predictions. Even though we have chosen relatively simple geometry in our simulations, practical adsorption beds can be of complex 3D shapes for which only 3D modeling is valid. For example adsorption systems for submarines or proposed on-board carbon-capture systems for busses and cars have complex shapes to space limitations. The main disadvantage of using 2D/3D models is longer time of running the required simulation in comparison to one-dimensional models.

The research will also highlight the advantage of utilizing Mg-MOF-74 for CO_2 separation and will explore the optimal TSA performances by finding out appropriate regeneration periods.

2. Experimental breakthrough setup

The CO_2 breakthrough separation of Mg-MOF-74 was tested using a home-made dynamic CO_2/N_2 breakthrough setup as shown in Fig. 1. The system consists of a fixed adsorbent bed column, feed CO_2 and N_2 cylinders, two gas regulators with dual pressure gauges and output control valves, two mass flow controllers (one was calibrated for CO_2 flow and the other was calibrated for N_2), two check valves (to control the flow in one direction), a bypass line (for calibrating the mass spectrometer from the feed gas mixture, Bourdon absolute pressure gages. The heard of the instrumentation system is an *environmental* quadruple mass spectrometer especially procured to analyze the output concentration of outflowing gases from the test bed. A temperature controlled heater jacket and a vacuum pump have been specified for desorption process. Some carefully placed valves and by-pass tubes are designed to control the flow and facilitate the running of different test with little delay. All pipes and fittings were made of stainless steel to minimize the effect of corrosion on the breakthrough system.

The tubular fixed bed had an inner diameter of 4 mm, an outer diameter of 6 mm and 7 cm long. It was filled with Mg-MOF-74 (about 0.26 g, virgin powder shape). Firstly, the samples were pre-treated by heating them at about 423 K under vacuum, for 24 h to remove trapped gases and moisture inside the adsorbent. The experiments were performed at ambient conditions to simulate actual flue gasses (from plants or cars). The mixed gas flow rate was 10 sccm (20% CO_2 and 80% N_2). The N_2/CO_2 gasses are mixed well through a long spiral tube section before feeding in the adsorbent bed. A small sample of the outflowing gasses is pulled through a capillary stainless steel tube (1/16″ inner diameter) by a vacuum pump to the mass spectrometer. Moreover, a heater jacket covering the adsorbent bed to raise the temperature of the adsorbent material for evacuating the bed from trapped gasses quickly.

3. Numerical modeling methods

3.1. Adsorbent bed and model description

The geometry of the adsorbent bed was a cylinder filled with adsorbent material (AC or Mg-MOF-74) as shown in Fig. 2. Axisymmetric two-dimensional (2D) (Fig. 2(a)) and symmetry three-dimensional (3D) (Fig. 2(b)) beds have been considered for modeling in this study. The 3D bed is presented by Polar Coordinate system (r, θ, z). Including angular direction (θ) is to calculate the partition of heat and mass that transfer in circular path. The radial direction, r, is reduced to y direction in 2D because the angle θ is zero, therefore 2D is presented by Cartesian Coordinate system (x, y). The x-direction in 2D is the same z-direction in 3D. The bed geometry and adsorbent properties will be described later.

The simulation model is based on the momentum, mass and energy conservation equations. The CFD model has been developed using User Define Function (UDF, written in C language) hooked to Ansys-Fluent software [39] to estimate gases adsorption quantities and adjusts the source terms of mass, momentum and energy equations. The model is valid for multi-dimensional and various geometries.

For all studied cases, the following assumptions are adopted:

- the gas phase obeys ideal gas law and
- the flow is laminar (Re < 10),
- the porous media is homogenous,
- the physical properties of the adsorbents are constant, and
- the Linear Driving Force (LDF) model is used to account for the mass transfer rate during the adsorption process.

In addition, the isotherms were accurately fitted from the experimental ones according to the appropriate approaches like Toth and Dual-site Langmuir.

3.2. Mass conservation equation

The mass conservation equation calculates the local mass fraction of each species through the solution of the convection-diffusion equation of the all species as the following:

$$\varepsilon\frac{\partial(\rho y_i)}{\partial t} + \nabla.(\rho\vec{v}y_i) = -\nabla(-\varepsilon\rho D_{disp,i}\nabla y_i) - (1-\varepsilon)\rho_p M_i\frac{\partial q_i}{\partial t} \quad (1)$$

where ρ (kg m^{-3}) is the gas density, y_i is the mass fraction of species i (CO_2 and N_2), $\vec{v}$ (m s^{-1}) is the velocity vector, ε is the bed porosity, $D_{disp,i}$ (m^2 s^{-1}) is the mass dispersion coefficient for species i, M_i (kg mol^{-1}) is the molecular weight of species i, q_i (mmol g^{-1}) is the adsorbent amount of component i, and t(s) is the time. ∂ is the symbol of partial derivation and ∇ is the symbol the differential operator; it services for (r, θ, z) in 3D and (x, y) in 2D. The first and second terms in the left hand side (Eq. (1)) are the unsteady mass and mass advection, respectively. Whereas, the first and second terms in the right hand side (Eq. (1)) are the mass diffusion and the adsorption source, respectively.

The overall mass balance is

$$\varepsilon\frac{\partial(\rho)}{\partial t} + \nabla.(\rho\vec{v}) = -(1-\varepsilon)\rho_p\sum_i M_i\frac{\partial q_i}{\partial t} \quad (2)$$

3.3. Momentum conservation equation

The momentum equation of the gases flow can be expressed as

$$\varepsilon\frac{\partial(\rho\vec{v})}{\partial t} + \nabla.(\rho\vec{v}\vec{v}) = -\nabla P + \nabla.\bar{\bar{\tau}} + \rho\vec{g} + S_i \quad (3)$$

where P (Pa) is the operating pressure, $\bar{\bar{\tau}}$(N m^{-2}) is the stress sensor, $\vec{g}$ (m s^{-2}) is the gravity acceleration vector, and S_i (N m^{-3}) is the momentum source tem in the porous media. It is calculated from Ergun equation including inertia and viscus resistances as:

$$S_i = -\left(\frac{\mu}{\kappa}v_i + C_2\frac{1}{2}\rho|\vec{v}|v_i\right) \quad (4)$$

where μ (Pa s) is the gas dynamic viscosity, 1/κ (m^{-2}) is the porous media viscous resistance, C_2 (m^{-1}) is the inertial resistance, $|\vec{v}|$ is the value of the velocity vector, and v_i is the velocity component in i-direction.

3.4. Energy conservation equation

The energy equation for CO_2 separation shows the balance between the energy stored in the adsorbent bed and the change in energy due to convective flow, pressure work, thermal diffusion and advection as well as the energy released/consumed as a consequence of adsorption/desorption processes. It could be written as:

$$\frac{\partial}{\partial t}[\varepsilon\rho E_g + (1-\varepsilon)\rho_p E_s] + \nabla.[\vec{v}(\rho E_g + P)] = \nabla.\left[k_{\text{eff}}\nabla T - \sum_i h_i\vec{J_i} + \bar{\bar{\tau}}.\vec{v}\right] + (1-\varepsilon)\rho_p\sum_i \Delta H_i\frac{\partial q_i}{\partial t} \quad (5)$$

where E_g (J m^{-3}) is the total gas energy, E_s (J m^{-3}) is the total adsorbent energy, ΔH (J mol^{-1}) is the heat of adsorption which is different from material to another and sometimes also varies with variation of gas adsorbed amounts, T (K) is the equilibrium temperature, h_i (J kg^{-1}) is the sensible enthalpy ($h = \sum_i y_i h_i$), and $\vec{J_i}$ (kg m^{-2} s^{-1}) is the diffusion flux of the gas component i.

The parameter k_{eff} is the effective conductivity of the adsorbent bed and can be expressed as:

$$k_{\text{eff}} = \varepsilon k_g + (1-\varepsilon)k_s \quad (6)$$

where k_g and k_s (W m^{-1} K^{-1}) are the thermal conductivities of the gas mixture and adsorbent, respectively.

For the wall metal, the energy equation through the walls depends upon the balance of heat stored in the wall and the heat diffusion through it as follows.

$$\frac{\partial}{\partial t}(\rho_w C_w T_w) = \nabla(k_w\nabla T_w) \quad (7)$$

where ρ_w (kg m^{-3}) is the wall density, C_w (J kg^{-1} K^{-1}) is the wall heat capacity, T_w (K) is the local temperature of the wall, and k_w (W m^{-1} K^{-1}) is the thermal conductivity of the wall material.

3.5. Adsorption isotherm and kinetics models

The equilibrium adsorption isotherms are presented by different models according to the accuracy of the fitting from the experimental isotherms. Toth and Dual-site Langmuir models are exploited for gases equilibrium adsorption.

Toth model:

$$q_i^* = \frac{q_{m,i}K_{eq,i}y_i P}{(1 + (K_{eq,i}y_i P)^{ni})^{\left(\frac{1}{ni}\right)}} \quad (8)$$

where $q_{m,i}$ (mmol g^{-1}) is the maximum adsorbed amount of species i, $K_{eq,i}$ (Pa^{-1}) is an adsorption constant which can be calculated as a function of temperature (Eq. (9)), and ni is the adsorption constant.

$$K_{eq,i} = k_0 e^{-\left(\frac{\Delta H}{RT}\right)} \quad (9)$$

where k_0 (Pa^{-1}) is a temperature-independent constant.

Dual-site Langmuir model:

$$q_i^* = \frac{q_{m,i1}K_{eq,i1}y_i P}{1 + K_{eq,i1}y_i P} + \frac{q_{m,i2}K_{eq,i2}y_i P}{1 + K_{eq,i2}y_i P} \quad (10)$$

where $q_{m,i,1}$ and $q_{m,i,2}$ (mmol g^{-1}) are to present the maximum adsorbed amount of species i, $K_{eq,i,1}$ and $K_{eq,i,2}$ (Pa^{-1}) are adsorption constants that depend on the adsorbent temperature.

The adsorption kinetics are evaluated by a linear driving force (LDF) model as follows.

$$\frac{\partial q_i}{\partial t} = k_{L,i}(q_i^* - q_i) \quad (11)$$

The parameter q_i (mmol g^{-1}) presents the actual adsorbed amount while q_i^* (mmol g^{-1}) is the equilibrium adsorbed amounts. $k_{L,i}$ (s^{-1}) is the adsorption time constant and is estimated from the film, macroporous, microporous resistances of the gases passing porous materials as:

$$\frac{1}{k_{L,i}} = \frac{r_p q_{0,i}}{3k_{f,i}C_{0,i}} + \frac{r_p^2 q_{0,i}}{15\varepsilon_p D_{p,i}C_{0,i}} + \frac{r_c^2}{15D_{c,i}} \quad (12)$$

where $q_{o,i}$ and $C_{0,i}$ (mol m^{-3}) are the values of the concentrations at the solid and gas phases, respectively, r_p (m) is the adsorbent particle radius, ε_p is the particle porosity, and r_c is the adsorbent crystal radius. $k_{f,i}$, $D_{p,i}$ and $D_{c,i}$ are the film mass transfer coefficient, macroporous diffusion coefficient, and microporous diffusion coefficient, respectively, for a component i. The evaluation of these coefficients were explained in [25,40]. The last term in Eq. (12) is the most dominant term to evaluate LDF parameters for Mg-MOF-74.

3.6. General boundary conditions

3.6.1. External walls

The heat transfer between the bed wall and the ambient can be expressed as

$$k_w\left(\frac{\partial T_w}{\partial n}\right)_w = h_{ext}(T_w - T_{amb}) + \sigma(T_w^4 - T_{amb}^4) \quad (13)$$

where n (m) is the normal, h_{ext} (W m^{-2} K^{-1}) is the external heat transfer confident, ε is the thermal emissivity, σ (W m^{-2} K^{-4}) is Steffen Boltzmann coefficient.

The heat transfer from the bed wall to the ambient relies on the heat transfer coefficient which may be calculated from Nusselt number using the following correlation [41]:

$$Nu = \frac{h_{ext} D_0}{k_{air}} = \left[0.60 + 0.387 \frac{Ra^{1/6}}{\left[1 + \left(\frac{0.559}{Pr_{air}}\right)^{9/16}\right]^{8/27}} \right]^2 \quad (14)$$

where D_o (m) is the external wall diameter, k_{air} ($Wm^{-1}K^{-1}$) is the thermal conductivity of the air at average temperature (of both the wall and the ambient temperatures), Pr_{air} is the air Prandtl number, Ra is Rayleigh number at average temperature.

For adiabatic walls:

$$\left(\frac{\partial T_w}{\partial n}\right)_w = 0 \quad (15)$$

3.6.2. Interfaces between walls and adsorbent

The convection heat transfer through the interface between the bed and wall is estimated by the local heat conduction Eq. (16).

$$k_{\text{eff}} \left(\frac{\partial T}{\partial n}\right)_w = h_{int}(T - T_w) = k_{\text{local}} \left(\frac{\partial T}{\partial n}\right)_{local} \quad (16)$$

where h_{int} ($W m^2 K^{-1}$) is the internal convection heat transfer coefficient calculated automatically by Fluent from the last term in Eq. (16). Also

$$\nabla y_i = 0 \quad (17)$$

3.6.3. Inlet boundary conditions

The specific values of pressure, temperature and flow rate/velocity at the inlet are given in Tables 1 and 3. Mass and heat transfer at the bed inlet could be expressed as the diffusion quantities in a balance to the advection ones.

$$-\varepsilon D_{i,m} \nabla y_i = \vec{v}\,(y_i|_- - y_i|_+) \quad (18)$$

$$-\varepsilon k_{\text{eff}} \nabla T = \vec{v}\,\rho(h_i|_- - h_i|_+) \quad (19)$$

3.6.4. Outlet boundary conditions

The specific values of pressure, and temperature at the outlet are given in Tables 1 and 3.Mass and heat fluxes at the outlet can be written as:

$$\nabla y_i = 0 \quad (20)$$

$$\nabla T = 0 \quad (21)$$

3.6.5. Centerlines (in 2D) and symmetry planes (in 3D)

Mass and heat fluxes at the axisymmetric axis and symmetry planes are

$$\nabla y_i = 0 \quad (22)$$

$$\nabla T = 0 \quad (23)$$

3.7. Materials properties

The materials used in the models were adsorbents (AC and Mg-MOF-74), gases (CO_2 and N_2), and stainless steel wall. So that the thermal properties for each species and wall material have been taken as a polynomial equation as a function of temperature (see Supporting Information: Eq. (S1)–(S3), Table S1). The gas mixture density has been calculated using ideal gas law, thermal heat capacity has been estimated from mixing-law, and the thermal conductivity and viscosity have been evaluated by mass-weighted-mixing-law. These all properties are shown in the next equations.

The mixture gas heat capacity is expressed by mixing-law as:

$$C_p = \sum_i x_i C_i \quad (24)$$

where x_i is the molar fraction of species. The thermal inertia of the bed can be estimated as|:

$$(\rho C_p)_{bed} = (\rho C_p)_{gas} + \rho_s (C_{p,s} + qMC_{p,g}) \quad (25)$$

The last term in Eq. (25) contains the heat capacity of adsorbed amounts. The molecular weight, M, should be taken in kg/mol.

The thermal conductivity and viscosity of the gas mixture are determined by the following mass-weight-mixing-law.

$$k = \sum_i \frac{x_i k_i}{\sum_j x_i \phi_{ij}} \quad (26)$$

$$\mu = \sum_i \frac{x_i \mu_i}{\sum_j x_i \phi_{ij}} \quad (27)$$

and

$$\phi_{ij} = \frac{\left[1 + \left(\frac{\mu_i}{\mu_j}\right)^{1/2} \left(\frac{M_j}{M_i}\right)^{1/4}\right]^2}{\left[8\left(1 + \frac{M_i}{M_j}\right)\right]^{1/2}} \quad (28)$$

The mass dispersion coefficient has been correlated for laminar low Reynolds number as [42]:

$$D_{disp,i} = 0.508 u \frac{d_p}{Re^{0.02}} \quad (29)$$

If the Reynolds number satisfies the condition of ($Sc\ Re\ \varepsilon \geq 0.3$), the appropriate correlation for the mass dispersion coefficient is [43]:

$$D_{disp,i} = 1.317 \frac{D_{m,i}}{\varepsilon} (\varepsilon ReSc)^{1.392} \quad (30)$$

3.8. Model validation and vacuum pressure swing adsorption (VPSA) cases

3.8.1. Model validation against experimental breakthrough experiment

Before we can use our models reliably for investigating the TSA process, we need to validate these models carefully against experimental data. Here we validate the main step of the TSA cycle which is the breakthrough separation step. Therefore, the results of the present

Table 1
Bed geometry and adsorption and thermal properties of AC bed [25].

Properties	Value
Bed length, L	0.171 m
Bed diameter, D	0.022 m
Bed wall thickness	0.0015 m
Bed density, ρ_s	546.24 kg m^{-3}
Adsorbent specific heat capacity, $C_{p,s}$	880 J $kg^{-1} K^{-1}$
Adsorbent thermal conductivity, k_s	0.63 W $m^{-1} K^{-1}$
Particle density, ρ_p	1138 kg m^{-3}
Adsorbent particle size, d_p	0.0038 m
Bed porosity, ε	0.52
Inlet velocity, u	0.00131 ms^{-1}
Inlet temperature, T	423 K
Outlet pressure, p	0 Pa (gauge)
Ambient temperature, T_{amb}	298 K (the bed was adiabatic)
CO_2 inlet molar fraction, x_{CO2}	0.2
N_2 inlet molar fraction, x_{N2}	0.8
Mass dispersion coefficient, D_{disp}	0.0000103 $m^2 s^{-1}$
Reynolds number, Re	0.2033
CO_2 adsorption time constant coefficient, $k_{L,CO2}$	0.032 s^{-1}
N_2 adsorption time constant coefficient, $k_{L,N2}$	0.128 s^{-1}
CO_2 adsorption heat, ΔH_{CO2}	−21840 J mol^{-1}
N_2 adsorption heat, ΔH_{N2}	−16310 J mol^{-1}

Table 3
Bed geometry and adsorption and thermal properties of Mg-MOF-74 bed.

Properties	Value
Bed length, L	0.07 m
Bed diameter, D	0.004 m
Bed wall thickness	0.001 m
Bed density, ρ_s	230.1 kg m^{-3}
Adsorbent specific heat capacity, $C_{p,s}$	900 J kg^{-1} K^{-1}
Adsorbent thermal conductivity, k_s	0.3 W m^{-1} K^{-1}
Particle density, ρ_p	911 kg m^{-3}
Average adsorbent particle size (virgin powder), d_p	0.0002 m
Bed porosity, ε	0.7417
Inlet flow rate, Q_F	10 sccm
Inlet temperature, T	297 K
Outlet pressure, p	0 Pa (gauge)
Ambient temperature, T_{amb}	297 K
CO_2 inlet molar fraction, x_{CO2}	0.2
N_2 inlet molar fraction, x_{N2}	0.8
CO_2 adsorption time constant coefficient, $k_{L,CO2}$	0.1182 s^{-1}
N_2 adsorption time constant coefficient, $k_{L,N2}$	0.3043 s^{-1}
CO_2 adsorption heat, ΔH_{CO2}	$-(42492.6-6568.83q+3973.75\,q^2-959.838\,q^3+69.1208\,q^4)$ J mol^{-1} $(0 < q < 7.5$ mmol $g^{-1})$
N_2 adsorption heat, ΔH_{N2}	-18000 J mol^{-1} [44]

model were compared with two experimental works. The first validation was done against the experimental work reported by Dantas [25] using activated carbon to separate CO_2 from CO_2/N_2 mixture at 101.3 kPa and 423 K, and the second validation was performed against the present experimental data for CO_2/N_2 separation using Mg-MOF-74 at 101.3 kPa and 297 K. The beds and system properties for the validation cases are described in below tables (Tables 1–6).

The equilibrium isotherm parameters in accordance to Toth model [25] are shown in Table 2.

The equilibrium isotherm parameters in accordance to Toth model at 297 K are shown in Table 4.

3.9. Temperature swing adsorption (TSA) cases

Temperature swing adsorption has been investigated using Mg-MOF-74 as adsorbent for the bed configuration described in Table 3. A single bed was used for the numerical modeling of the four steps of the TSA process, namely: feed, rinse, heating and cooling. The feed process consumed 250 s to feed the adsorbent bed with a mixture gas containing CO_2/N_2 (15% CO_2, 85% N_2 (vol. %)) at 101.3 kPa and 323 K. After bed feeding, pure CO_2 was introduced into the bed to rinse the remaining N_2 inside the bed voids; for about 40 s. The devoted times for feed and rinse steps were fixed through all cases taking into account breakpoint time, to avoid releasing CO_2 into the atmosphere. In our study we define the breakpoint time by the point at which the outlet CO_2 concentration is less than 5% of that at inlet. The breakpoint violation leads to emitting CO_2 to the atmosphere which should not occur. During the heating process, CO_2 was desorbed from the bed by increasing the bed temperature up to 393 K. Therefore, a significant amount of CO_2 has been removed from the bed. Before starting the next feed cycle, the bed should be cooled down by a certain cooling process. In our case, the cooling step has here been carried out by natural convection and radiation with the ambient surroundings. The bed and system properties for TSA cases are described in Table 5. The heating and cooling steps were investigated for optimal operation times (desorption times) as explained in Table 7. The detailed boundary conditions of the four steps are shown in Fig. 3. The first cycle of the all cases was devoted to fill the bed with CO_2 up to breakpoint using the feed and rinse steps. In order to reach quasi-steady state early, the feed time of the first cycle is taken longer than that of the others. During cooling step, the pressure decreases to be a vacuum; it depends on the cooling temperature and the remaining quantity of gases after heating step.

Dual-site Langmuir model have been used for predicting the equilibrium values of adsorbed amounts of CO_2 and N_2 at different temperatures as suggested by Manson [44]. Table 6 shows the Dual-site Langmuir parameters required for estimating the equilibrium CO_2 and N_2 adsorbed values.

3.10. TSA performance indices

The most important criteria of swing adsorption processes are the CO_2 purity and recovery. The CO_2 purity is the amount of pure CO_2 content (molar base) inside the produced CO_2 while CO_2 recovery is the ratio of the amount of produced carbon dioxide to that fed to the adsorbent bed.

The CO_2 purity and recovery may be calculated as below.

$$Purity\ of\ CO_2 = \frac{\int_{t_{startheating}}^{t_{startcooling}} F_{CO_2}dt}{\sum_i \int_{t_{startheating}}^{t_{startcooling}} F_i dt} \tag{33}$$

$$Recovery\ of\ CO_2 = \frac{\int_{t_{startheating}}^{t_{startcooling}} F_{CO_2}dt - \int_{t_{startrinse}}^{t_{startheating}} F_{CO_2}dt}{\int_{t_{startfeed}}^{t_{startrinse}} F_{CO_2}dt} c \tag{34}$$

and

$$F_i = Q_F C_i \tag{35}$$

where F_i (mol s^{-1}) is the molar flow rate of component i (CO_2 and N_2), Ci (mol m^{-3}) is the component concentration, and Q_F (m^3 s^{-1}) is the volumetric flow rate at the bed outlet.

For more useful performance analysis, the estimation of CO_2 productivity and TSA energy consumption are conducted as written in Eqs. (37) and (37).

$$Producivity of CO_2 = \frac{\int_{t_{startheating}}^{t_{startcooling}} F_{CO_2}M_{CO_2}dt - \int_{t_{startrinse}}^{t_{startheating}} F_{CO_2}M_{CO_2}dt}{t_{cycle}\,m_s} \tag{36}$$

where M_{CO2} (kg mol^{-1}) is the molecular weight of CO_2, t_{cycle} (hr) is the total time of one repeated cycle, and m_s (kg) is the adsorbent mass.

The energy consumption could be estimated as [45,46]:

Table 2
Equilibrium isotherm parameters for AC [25].

Gas species	q_m (mmol g^{-1})	K_0 (Pa^{-1})	n
CO_2	10.05	7.62e-10	0.678
N_2	9.74	6.91e-10	0.518

Table 4
Equilibrium isotherm parameters for Mg-MOF-74 at 297 K.

Gas species	q_m (mmol g^{-1})	K_0 (Pa^{-1})	n	$-\Delta H$ (J mol^{-1})
CO_2	11.4048	3.089e-11	0.4217	42,000
N_2	6.7072	9.36e-10	1	18,000

Table 5
Bed geometry and adsorption and thermal properties of Mg-MOF-74 bed.

Properties	Value
Bed length, L	0.07 m
Bed inner diameter, D_{in}	0.004 m
Bed wall thickness	0.001 m
Bed density, ρ_s	297 kg m^{-3}
Adsorbent specific heat capacity, $C_{p,s}$	900 J kg^{-1} K^{-1}
Adsorbent thermal conductivity, k_s	0.3 W m^{-1} K^{-1}
Particle density, ρ_p	911 kg m^{-3}
Adsorbent particle size, d_p	0.0002 m
Bed porosity, ε	0.674
CO_2 adsorption time constant coefficient, $k_{L,CO2}$	0.137 s^{-1}
N_2 adsorption time constant coefficient, $k_{L,N2}$	0.313 s^{-1}
CO_2 adsorption heat, ΔH_{CO2}	$-(42492.6 - 6568.83q + 3973.75\ q^2 - 959.838\ q^3 + 69.1208\ q^4)$ J mol^{-1} ($0 < q < 7.5$ mmol g^{-1})
N_2 adsorption heat, ΔH_{N2}	$-18{,}000$ J mol^{-1} [44]

$$E_{TSA} = \frac{1}{\eta}\int_{T_{bed,min}}^{T_{bed,max}} (m_s C_{p,s} + m_s q_{CO_2} M_{CO_2} C_{p,CO_2}) dT + \int_{T_{wall,min}}^{T_{wall,max}} m_w C_w dT_w + \int_{q_{min}}^{q_{max}} m_s \Delta H dq \quad (37)$$

where η is the heat source efficiency and assumed to be 0.8. The first integration is the sensible heat added to the adsorbent material and adsorbed CO_2, the second one is the heat consumed by the bed metal wall, and the third integration is for the heat consumed due to the desorption heat (isosteric desorption heat).

4. Results and discussion

In order to validate our models, the computer code results have been compared against the experimental data of the breakthrough experiments carried out in our laboratory. Note that the breakthrough experiment represents the main phase of a TSA cycle. Before carrying out the model validation, we need to carry a mesh-independence study in order to obtain numerically accurate results. This study is presented next.

4.1. Mesh independence

The 2D model domain for the adsorbent bed was meshed using structured quadrilateral elements. Grid independency was carried out using the following conditions. Bed material:Mg-MOF-74, total inlet flowrate of gas mixture is 20 sccm, the inlet temperature is 300 K and inlet pressure of 101.3 kPa for the adsorbent bed shown in Fig. 1. The thermal and adsorption properties are described in Tables 3 and 4. Fig. 4 shows the CO_2/N_2 concentration breakthrough (Fig. 4(a)) and volumetric flowrate at the bed outlet (Fig. 4(b)) for four different numerical grids (1120, 1320, 1600, and 1980 cells). The results for the different grids for both concentration ratio and outlet volume flow rates are almost identical indicating mesh-independent results hence any mesh size among the four used is satisfactory for numerically accurate simulations. For 3D bed, the cell size has been taken as that in 2D.

Note that the steady state value for the total outlet flow rate (~21.5 ccm) is above the inlet flow rate (20 ccm). This is due to the gas expansion due to the heat of adsorption during the breakthrough test.

Table 7
Cases of TSA regeneration times (heating and cooling).

Case	Heating time (s)	Cooling time (s)
1	200	200
2	250	200
3	300	200
4	200	300
5	200	400

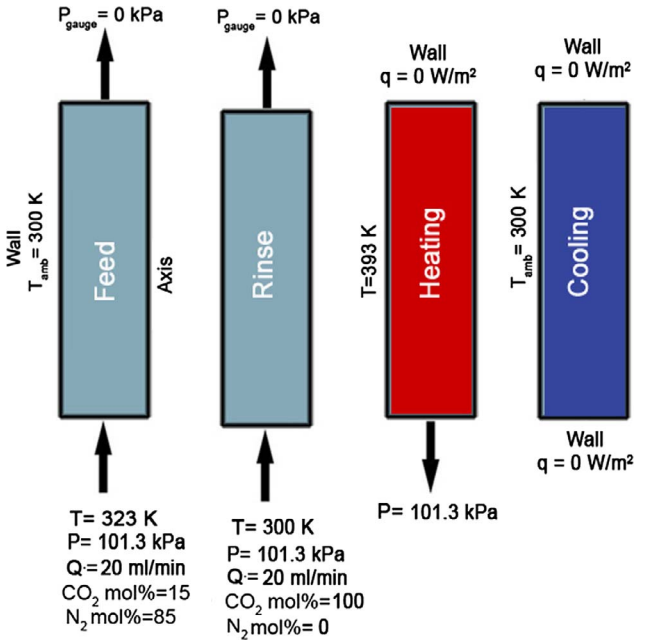

Fig. 3. Boundary conditions for four steps of TSA.

4.2. Model validation

The present numerical model results were validated against two experimental breakthrough data sets. The first validation case described in Tables 1 and 2 is concerned with separation of CO_2 from CO_2/N_2 mixture at high temperature (423 K) using activated carbon. The breakthrough curves of CO_2 and N_2 concentrations vs time at the bed outlet for both the experimental data of Dantas et al. [25], and the present numerical model results are shown in Fig. 5. It can be seen that

Table 6
Dual-site Langmuir model equilibrium isotherm parameters for Mg-MOF-74 [44].

Gas species	$q_{m,1}$ (mmol g^{-1})	$q_{m,2}$ (mmol g^{-1})	$K_{0,1}$ (Pa^{-1})	$K_{0,2}$ (Pa^{-1})	$-\Delta H_1$ (J mol^{-1})	$-\Delta H_2$ (J mol^{-1})
CO_2	6.8	9.9	2.44e-11	1.39e-10	42,000	24,000
N_2	14	–	4.96e-10	–	18,000	–

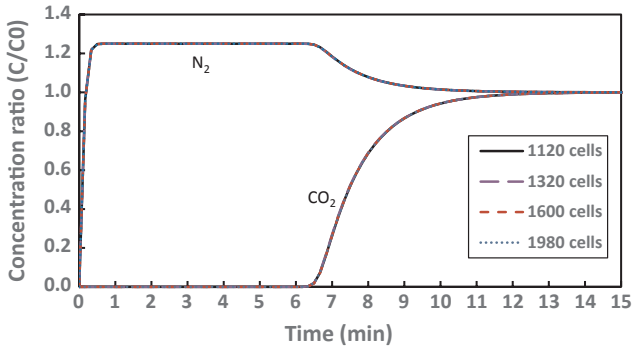

(a) CO_2/N_2 concentration ratios.

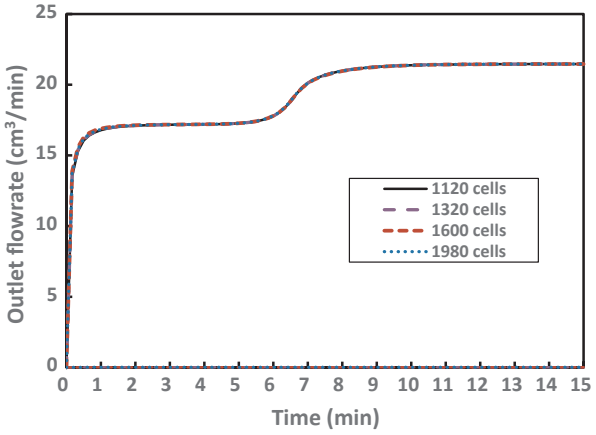

(b) Bed total outlet flowrate.

Fig. 4. CO_2/N_2 concentration ratio (a), and total outlet flowrate (b) profiles for different numerical meshes of 1120, 1320, 1690, and 1980 cells.

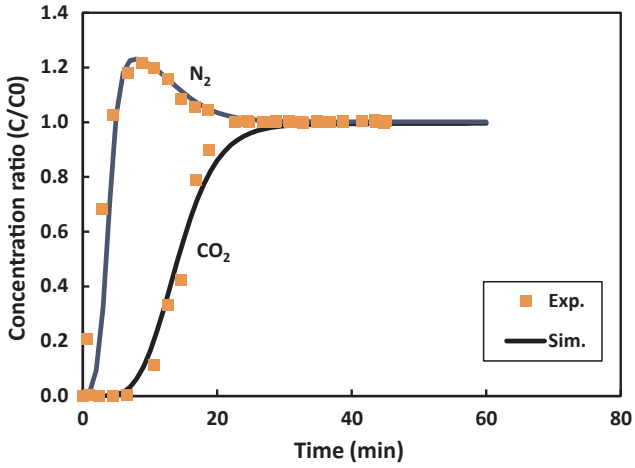

Fig. 5. Validation of numerical results against experimental data [25] for breakthrough CO_2/N_2 concentration ratio curves at the bed outlet during CO_2 adsorption process using activated carbon adsorbent at 301 K.

the numerically predicted CO_2 and N_2 concentration profiles are in good agreement with the experimental data. The results indicate that the concentration ratio of CO_2 was zero at the bed outlet for the first 7 min, while CO_2 is being adsorbed. As a result the concentration ratio (actual concentration normalized by inlet concentration) value of N_2 rose up to approximately 1.22 due to the absence of CO_2. As the adsorbent material gets saturated, the outlet concentration ratio of CO_2 increased up to 1 and the concentration ration of N_2 decreases down to 1.

The second validation is a comparison between the present

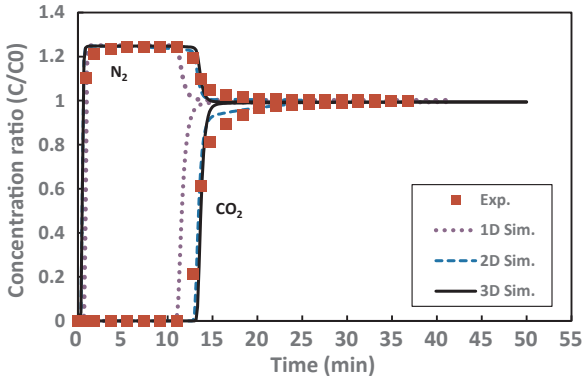

(a) CO_2/N_2 concentration ratios at the bed outlet.

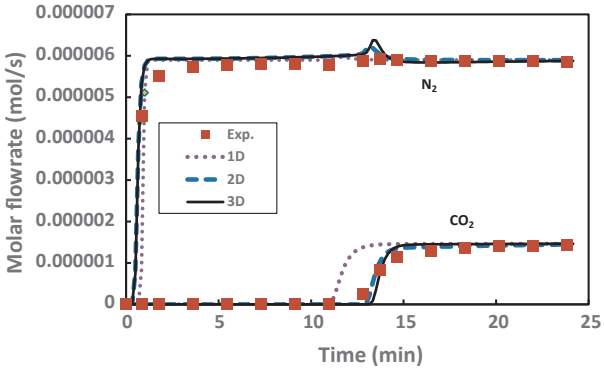

(b) CO_2/N_2 molar flowrates at the bed outlet.

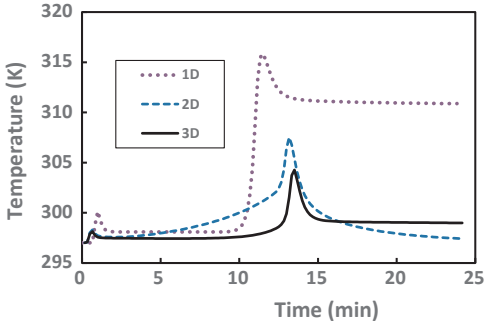

(c) Temperature profiles at the bed outlet.

Fig. 6. A comparison between present experimental and simulation (1D, 2D, and 3D) results of (a) breakthrough concentration ratio curves of CO_2/N_2, (b) CO_2/N_2 molar flowrate profiles, and (c) temperature profiles (simulation only) at the bed outlet during the adsorption process using Mg-MOF-74 at 297 K and 101.3 kPa.

experimental work results and 1D (using MATLAB), 2D and 3D simulations (using UDF-Fluent) at ambient temperature of 297 K. The 1D lumped model have been developed according to the frequently published model such as that reported by Dantas [25]. Fig. 6(a) shows the concentration ratio of CO_2/N_2 separation at the bed outlet using Mg-MOF-74 (see Tables 3 and for details 4). The CO_2/N_2 curves revealed an excellent agreement between the experimental results and the 2D and 3D numerical simulations. The transient outlet CO_2/N_2 molar flowrate values are shown in Fig. 6(b). As shown, the 2D and 3D results were closer to those of experimental work than the 1D numerical results, especially for CO_2. The temperature profiles for the three simulation cases are shown in Fig. 6(c). Generally, the temperature values at the bed outlet were not very high due to the bed was not adiabatic, and then the bed has exchanged the heat with the ambient through the bed wall. There is a small discrepancy between temperature values of 2D and 3D. In other words, the effect of flow, heat, and adsorption in θ-

direction is negligible whereas including that for r-dimension is significant when using cylindrical beds. On the other side, the 1D simulation had a significantly different temperature values comparing to those of 2D and 3D. The variation of temperature values of the three models can be explained by the treatment of the thermal diffusion in the different models. For the case we are treating the geometry is axisymmetric and the cooling around the bed (angular direction) is uniform, hence we need at least a 2D model to obtain accurate results. The main reason of the discrepancy between the 1D simulation and the experimental values of concentration ratio and CO_2 molar flowrate is due to ignoring the thermal diffusion term in the adsorbent energy equation and assuming constant thermal-physical properties. Moreover, this discrepancy is also due to the fact that the 1D model ignores the gradients in the radial direction and does not account for the mass and thermal diffusion in that direction. For these reasons, the temperature profile for the 1D model have the highest values (Fig. 6(c)) which lead to decrease the adsorption capacity and thereby; decreasing the adsorption stoichiometric time.

In summary, the 2D UDF-Fluent simulation is enough to carry out adsorption breakthrough simulations for this symmetric geometry with symmetric boundary conditions. Our 3D model was developed to model truly 3D situations such as columns with non-uniform boundary conditions around the periphery or non-symmetrical shapes where axi-symmetry would not be satisfied. As a check of our 3D model we have chosen to include the results of the axi-symmetric case, which should be the same as the 2D model results.

Finally we should note that the amount adsorbed and the saturation of the bed and in turn the stoichiometric time (*usually termed by adsorption researchers as the breakthrough time*); are all strong functions of temperature. Under physical adsorption, the higher the temperature, the lower is the amount adsorbed and the shorter is the break-through time. Therefore if the model predicts a higher temperature then we expect the breakthrough time to be shorter as depicted in Fig. 6a and b. The 1D model has predicted higher temperature which results in a shorter break-through time. The 2D and 3D models have predicted almost the same temperature (except for some numerical errors), and in turn the breakthrough times were almost the same.

4.3. A comparison between 2D and 3D TSA simulations

Temperature swing adsorption is an important technology for CO_2 adsorption. It could take its merits from the capability to supply the needed regeneration heat from cheap sources like waste heat.

The 2D and 3D beds, shown in Figs. 1 and 2 and described in Table 6, have been investigated to perform TSA for CO_2 separation from CO_2/N_2 mixture. TSA was presented by 4 steps namely: feed (250 s), rinse (40 s), heating (200 s), and cooling (300 s). The recycled CO_2 uptake profile is shown in Fig. 7 for both 2D and 3D simulations. About 3.3 mmol g^{-1} was successfully recycled by heating the bed to about 393 K. CO_2 uptake (Fig. 7(a)) showed a superior closeness between 2D and 3D simulation modeling. The bed average pressure history during two cycles for both 2D and 3D is shown in Fig. 7(b). It is clear that the pressure values were about 101.3 kPa during feed, rinse, heating steps while they dropped down to almost 8.5 kPa during cooling process due to the decrease of temperature as bed terminals were closed. The difference between the pressure values of both 2D and 3d was very small.

Fig. 8 is dedicated to show 2D and 3D temperature contours for one repeated cycle of TSA during selective times (at 2683, 2816, 2936, 2976, 3056, 3176, 3326, and 3476 s) for all steps. During the feed process (at 323 K), the cooled bed (immediately after a previous cooling step) was cooled down again (from about 324 K to about 314 K) during feed step due to keeping the bed exposed to the ambient. The temperature values increased for some degrees during the rinse step as a result of more CO_2 adsorption. The heating process raised the bed temperature up to 393 K in pursuit of extracting the majority of the adsorbed CO_2 from the bed. After that, the cooling process has taken place to cool down the bed before starting a new feed process. It is noticed that there was a small difference between 2D and 3D temperature contours due to respecting the thermal diffusion through the three dimensions in 3D simulation. However, this small difference in temperature values does not impinge on the TSA performance. Fig. 9 demonstrates the CO_2 molar fraction through the bed. The high values of CO_2 molar fraction at the start of the feed step represented those values at the end of cooling step of the previous cycle (Fig. 9(a)). The CO_2 molar fraction values have increased slowly along the bed during the feed step to the value about 0.15 (the same value of CO_2 in the inlet gas mixture). After that, the values increased dramatically to about 1 (as shown in the 1st half of the bed at 2976 s) by the end of the rinse process due to feeding pure CO_2, and then the CO_2 molar fraction amounts have persisted at high levels (> 0.85) during the heating and cooling processes (Fig. 9(a)). That it because of the majority of N_2 amounts were rinsed during rinse process. For more explanation, the CO_2 molar fraction values, along the x-axis passing through the middle of the 2D bed for the end period of each four-step (for one repeated cycle), are represented in Fig. 9(b). The CO_2 molar fraction was about 15% at the first half of the bed, for the end period of the feed step, while the rest of the bed has values decreased down to about 0.045 at the bed exit. The values of CO_2 molar fraction increased to the maximum level (1) at the end of the rinse step whereas the values at the third have decreased sharply. The rinse step was not elongated to fill the rest of the bed by CO_2 in order to avoid releasing CO_2 to the ambient. At the end of the rinse step, the bed was filled mainly with CO_2 while a little amount of N_2 was remained in the bed void. During heating step, the CO_2 released from the adsorbent to fill out the bed void and then left the bed,

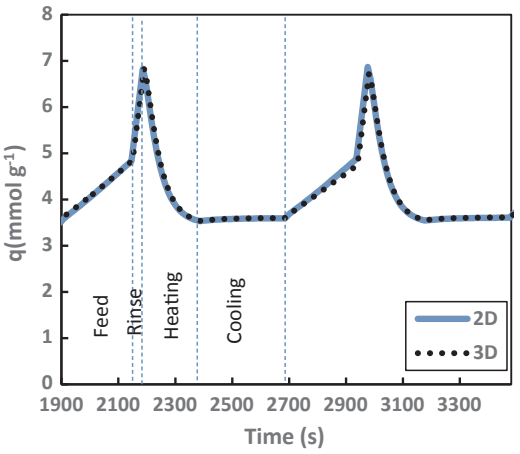

(a) Bed average CO_2 uptake.

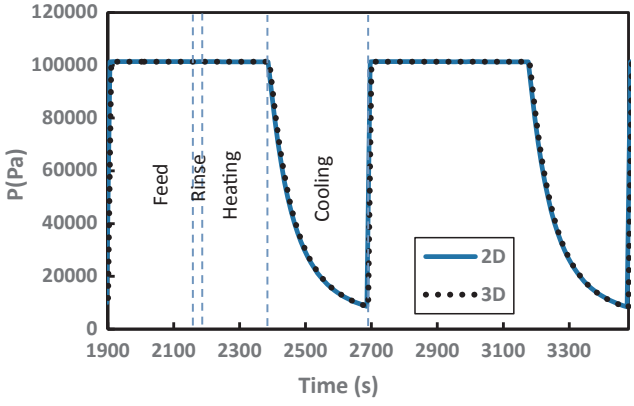

(b) Bed average pressure.

Fig. 7. Comparison between 2D and 3D in terms of (a) bed average CO_2 uptake and (b) bed average pressure during 2 cycles.

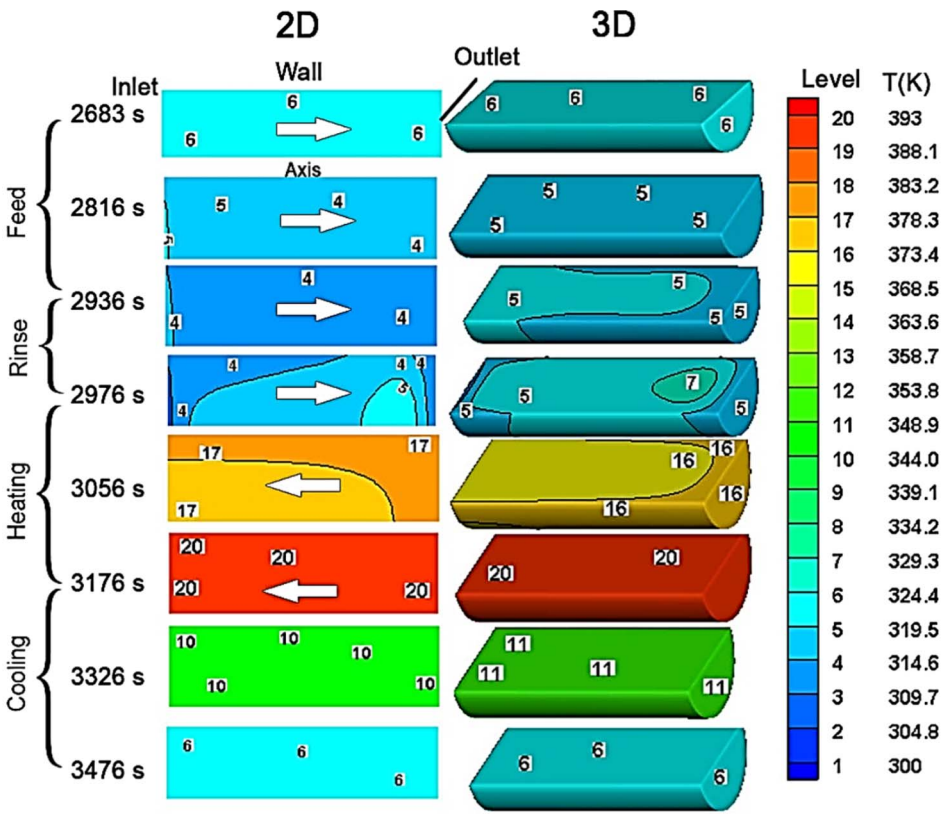

Fig. 8. A comparison of temperature contours of the bed between 2D and 3D TSA during a steady state cycle.

so that the molar fraction of CO_2 was close to 100%. During the cooling process, little amounts of CO_2 has only remained in the bed void with very little amounts of N_2. Because of decreasing the bed temperature, the adsorbent adsorbed again some of CO_2 from the bed void. Therefore, the values of CO_2 molar fraction minimized to about 85% at the end of the cooling step. The carbon dioxide uptake contours (2D and 3D) are shown in Fig. 10. The adsorbent (Mg-MOF-74) could be filled by about 5 mmol g^{-1} at the end of the feed process, and increased to the maximum level (about 7.5 mmol g^{-1}) at the end of the rinse process. The heat process was then able to minimize the values of CO_2 uptake to about 3.4 mmol g^{-1}).

4.4. TSA cases

Temperature swing adsorption is studied for 11 cycles to demonstrate the CO_2 cycling stability using the same 2D model for the bed shown in Fig. 2 by applying 4 steps including feed, rinse, heating, and cooling for about 250, 40, 200, 400 s, respectively. Fig. 11 shows the temperature profile at the middle of the bed during 11 repeated cycles. The temperature values increased to about 313 K during the 1st rinse step due to adsorbing pure CO_2 which is an exothermic process. The temperature values, then, increased again to about 391 K at the end of the heating process and subsequently cooled down to about 324 K at the end of cooling processes. Temperature values dropped to about 313 K after the feed and rinse processes as the bed was cooled down by the surrounding ambient. Generally, the temperature values fluctuated between 393 K and 313 K during all the TSA cycles. Quasi-steady cycles could be assumed from the sixth cycle. The history of CO_2/N_2 molar flow rates are shown in Fig. 12 for 11 consecutive cycles. The N_2 dominated at the bed outlet during feed and rinse steps while the CO_2 was dominant during the heating processes due to the desorption process.

Fig. 13 exhibits the history of the bed average value of CO_2 uptake during 11 cycles. Almost a quantity of 3.3 mmol g^{-1} was successfully recycled. The sharp lines during adsorption process indicated the CO_2 uptake at the rinse step as the CO_2 adsorption process occurred at high CO_2 pressure of 101.3 kPa, compared to low pressure of 15.2 kPa during the feed step.

In order to investigate the impact of heating and cooling times on the TSA performance, 5 cases (see Table 7) were compared in terms of CO_2 purity, recovery, and productivity as well the energy consumed during the regeneration process, assuming that the efficiency of the heat source is 0.8. The comparison was done when the cycles reached quasi-steady state for every case. Fig. 14 shows the CO_2 purity, recovery and productivity for different heating times between 200 and 300 s.

The increase of heating time, to some extent; improved the CO_2 recovery (from 69.3% to 70.5%) and did not affect much the purity (from 95.5% to 94.8%). Actually these minor changes in the CO_2 purity and recovery is not significant at all, indicating that the lowest time (200 s) is sufficient for the heating step. The CO_2 productivity is highest at 200 s heating time. More heating reduces the productivity from 0.253 to 0.228 kg_CO_2 hr^{-1} kg_MOF^{-1} (Fig. 14). This is because more heating results in less adsorption of CO_2.

The effect of cooling time on the TSA performance is shown in Fig. 15. It is obvious that the increase of the cooling time (from 200 s to 400 s) have increased the CO_2 recovery (dramatically from 52.8% to 73.2%), purity (slightly from 94.2% to 95.2%) and productivity (slightly from 0.221 to 0.24 kg_CO_2 hr^{-1} kg_MOF^{-1}). There is an optimal CO_2 productivity about 0.253 kg_CO_2 hr^{-1} kg_MOF^{-1} at cooling time of 300 s.

The calculated power consumption of CO_2 separation utilizing TSA are shown in Figs. 16 and 17 for both heating and cooling times. The power consumption values increased marginally (from 2.57 to 2.59 MWh tonne_CO_2^{-1}) by increasing the heating periods (from 200 to 300 s) as shown in Fig. 16. Fig. 17 depicts the power consumed due to extending the cooling time from 200 to 400 s. The values of the power consumed have declined by (6.3%) from 2.68 to 2.51 MWh tonne_CO_2^{-1} as giving a good reason for extending the cooling time.

The most important point in this scenario is that the power consumption for the adsorbent/adsorbate is much lower than that

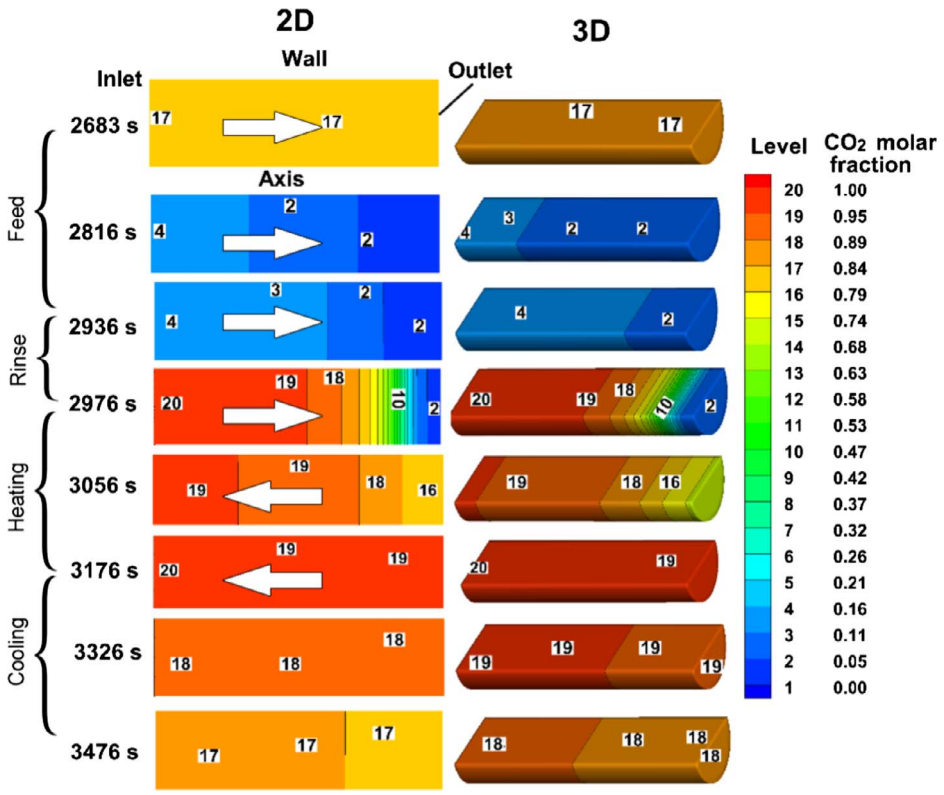

(a) 2D and 3D CO_2 molar fraction.

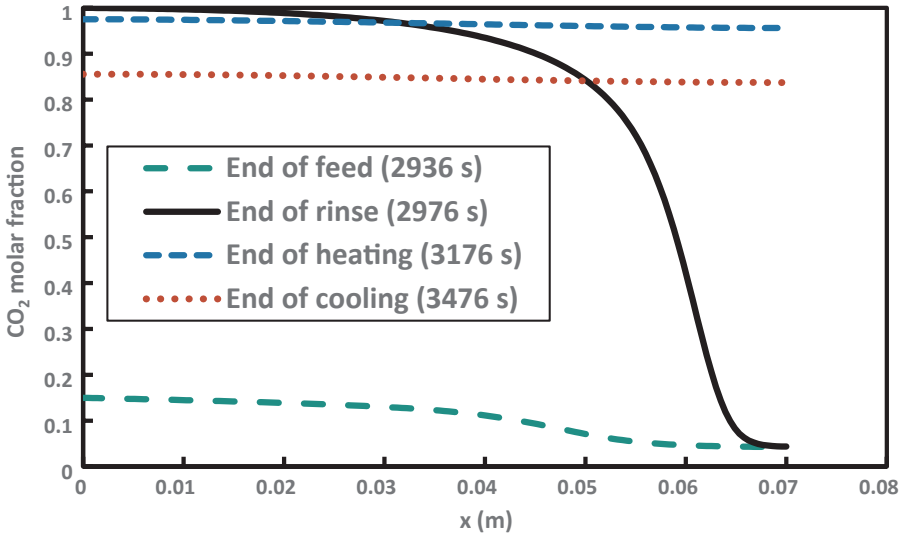

(b) Axial CO_2 molar fraction profiles.

Fig. 9. CO_2 molar fraction for one repeated TSA cycle in terms of (a) 2D and 3D contours and (b) axial profile at the bed middle along x-axis (for 2D).

consumed by the metal walls owing to the metal wall has a much higher thermal inertia than the adsorbent (Mg-MOF-74) and gases (CO_2 and N_2). The difference between the total power consumption and that when ignoring the metal walls power consumption was about 22 times. Therefore, it is recommended here to use wall materials that have low thermal capacity, low density and high thermal conductivity and the wall thickness should be as thin as possible.

Our study has also investigated the effect of the wall thickness on the performance measures. The wall thickness (1 mm) to internal diameter (4 mm) ratio of the studied bed was about 0.25 which is available in a market for stainless steel quarter inch tubes. However, this ratio is very small in large diameter tubes. Another wall thickness value of 0.5 mm was investigated ($t_w/D_{in} = 0.125$).

It is shown in Fig. 18 that the increase of wall thickness decreased the CO_2 purity, recovery and productivity. Fig. 19 confirms that the power consumption was about 0.664 MWh tonne_$CO_2$$^{-1}$ for 0.125 t_{wall}/D_{in}. The power consumption has been magnified to about 2.5 MWh tonne_$CO_2$$^{-1}$ for the higher thickness due to increasing the thermal inertia of the bed wall.

Hence, the best case was that associated with the smaller wall thickness and desorption periods of 200 s for heating and 400 s for cooling. It showed that the optimum CO_2 purity, recovery, productivity,

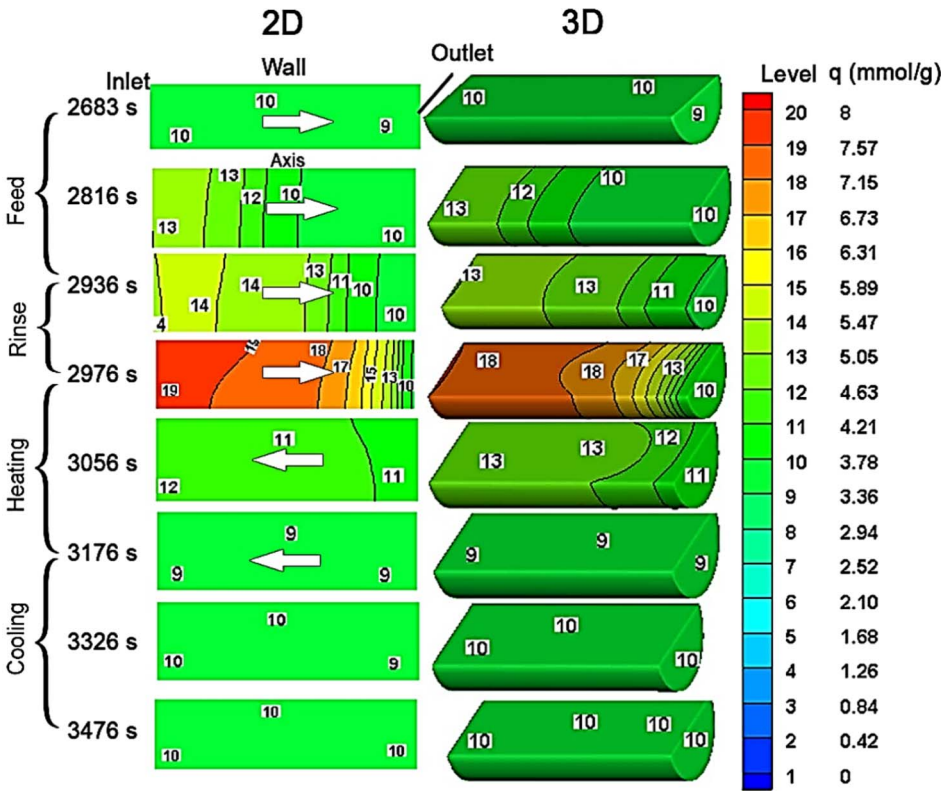

Fig. 10. A comparison of CO_2 uptake contours between 2D and 3D TSA during a steady state cycle.

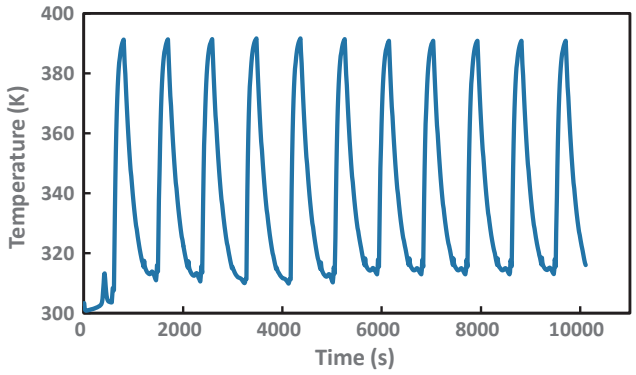

Fig. 11. Temperature profile at the middle of the bed for 11 TSA cycles (feed = 250 s, rinse = 40 s, heating = 200 s, and cooling = 400 s).

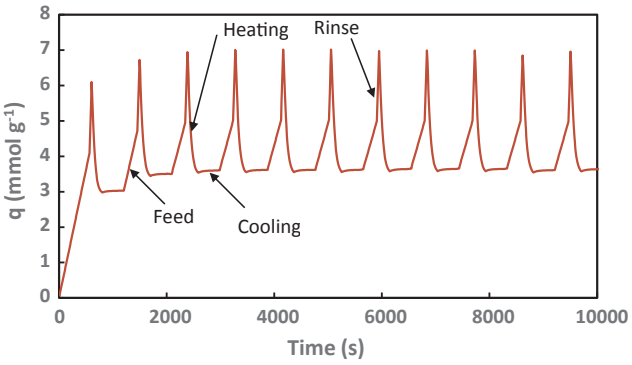

Fig. 13. Bed average CO_2 uptake of 11 TSA cycles (feed = 250 s, rinse = 40 s, heating = 200 s, and cooling = 400 s).

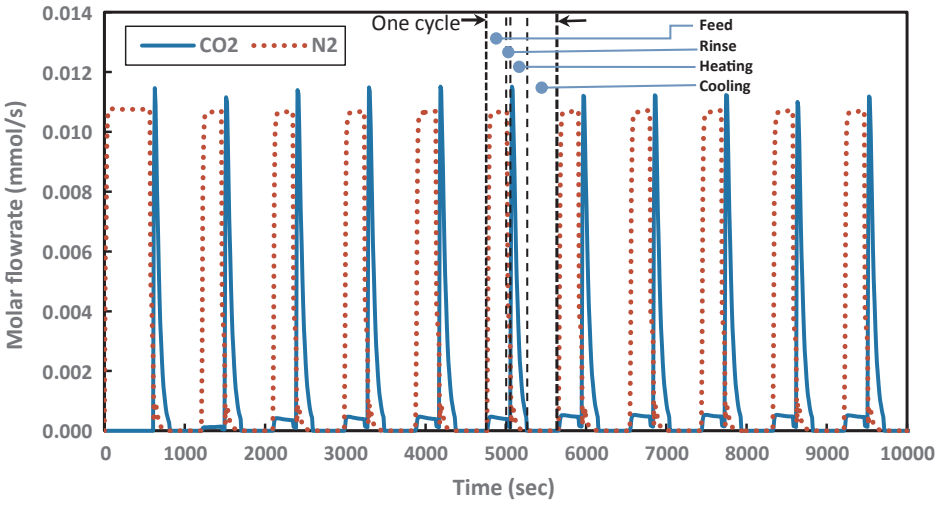

Fig. 12. CO_2/N_2 molar flowrate of 11 TSA cycles (feed = 250 s, rinse = 40 s, heating = 200 s, and cooling = 400 s).

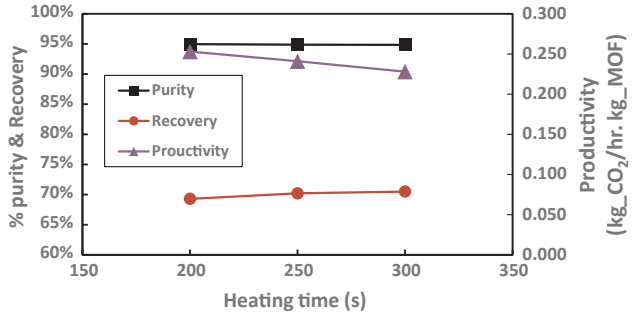

Fig. 14. Effect of heating time on CO_2 purity, recovery and productivity of TSA (feed = 250 s, rinse = 40 s, and cooling = 300 s).

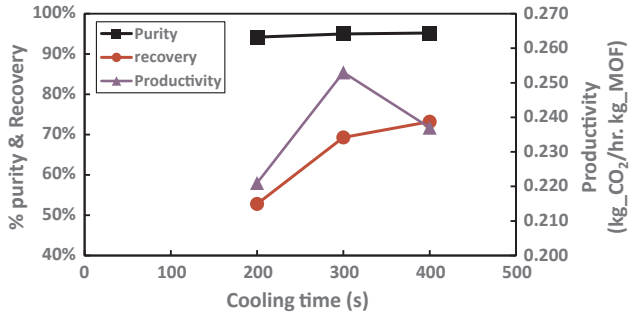

Fig. 15. Effect of cooling time on CO_2 purity, recovery and productivity of TSA (feed = 250 s, rinse = 40 s, and heating = 200 s).

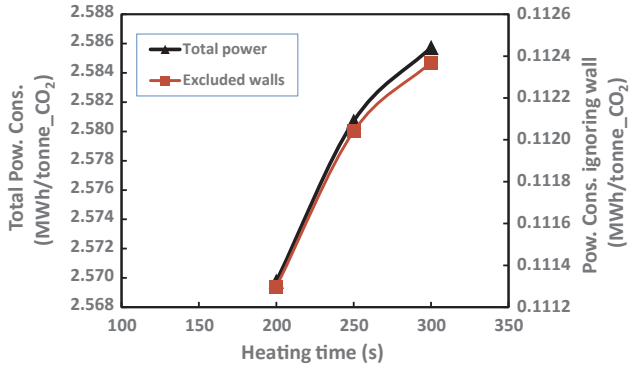

Fig. 16. Effect of heating time on TSA power consumption (feed = 250 s, rinse = 40 s, and cooling = 300 s).

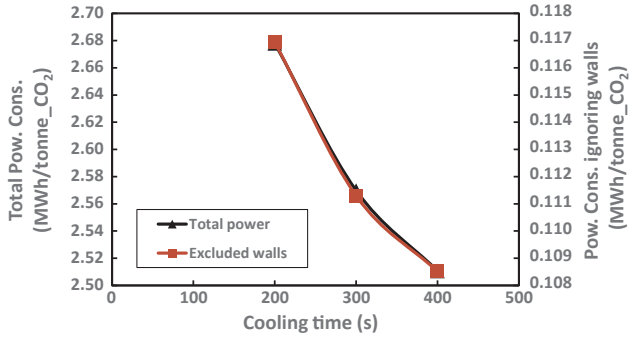

Fig. 17. Effect of cooling time on TSA power consumption (feed = 250 s, rinse = 40 s, and heating = 200 s).

power consumption were about 96.22%, 86.5%, 0.279 kg_CO_2 hr^{-1} kg_MOF^{-1} and 663.8 kWh tonne_CO_2^{-1}, respectively.

Table 8 shows a comparison of CO_2 separation performances between the present TSA and some swing adsorption processes and

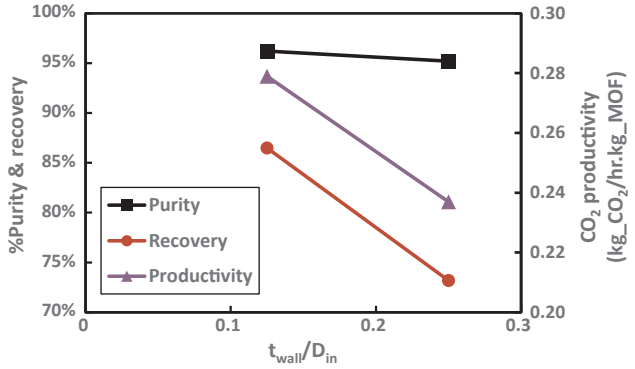

Fig. 18. Effect of wall thickness to internal diameter of the bed on CO_2 purity, recovery and productivity for TSA (feed = 250 s, rinse = 40 s, heating = 200 s, and cooling 400 s).

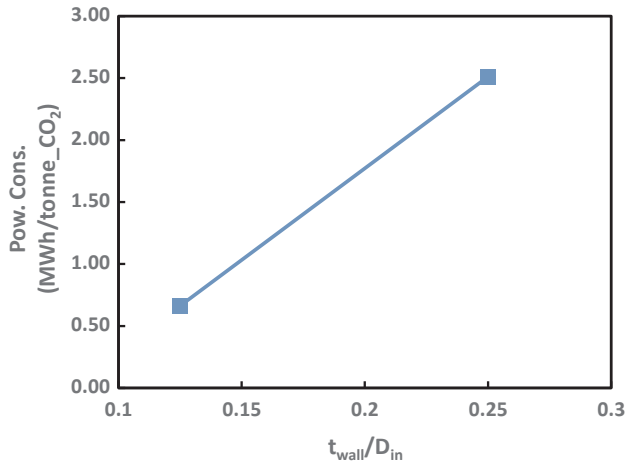

Fig. 19. Effect of wall thickness to internal diameter of the bed on TSA power consumption (feed = 250 s, rinse = 40 s, and heating = 200 s and cooling 400 s).

adsorbents reported in the literature. The present TSA gives a very good improvement in CO_2 productivity with high purity and productivity and reasonable power consumption. These enhancements have been obtained because of utilizing Mg-MOF-74 as an excellent CO_2 adsorbent, and also by optimizing of the regeneration (desorption) time.

5. Conclusions

Temperature swing adsorption (TSA) for separating CO_2 from CO_2/N_2 mixture using Mg-MOF-74 has been numerically investigated in this work. A CFD model was developed using User-Defined-Function (written in C language) linked to Ansys-Fluent software. This was necessary to implement the adsorption models and adjust the source terms of mass, momentum and energy equations, since Fluent does not have an adsorption-desorption model. The developed model has been employed to carry out two and three dimensional simulations. The results of the developed UDF-Fluent have been validated against published breakthrough experimental data at high temperature conditions using activated carbon, and experimental data collected by the authors at ambient temperature (297 K) using Mg-MOF-74. The multidimensional modeling have shown that the 2D model is accurately enough to present the CO_2 separation process by TSA for the cylindrical geometry chosen. The temperature swing adsorption process have been implemented in five steps: pressurization, feed, rinse, blowdown, and purge with an operating temperature range between 300 and 393 K and inlet feed temperature of 323 K. The heating and cooling periods and the bed wall thickness have been varied to explore an optimum TSA performance. The optimal performance was obtained for low wall thickness of 0.5 mm, a heating time of 200 s and a cooling time of 400 s.

Table 8
A Comparison of CO_2 separation performances amongst different materials and processes.

Adsorbent	Process	CO_2 (vol.%)	%Purity	% Recovery	Productivity (kg_CO_2 hr^{-1} kg_Adsorbent^{-1})	Energy consumption(kJ kg_$CO_2{}^{-1}$)	Study	Ref.
13X-APG	VPSA	15.5–16.5	95.6	73–82.3	0.0387	1790–2140	Exp.	[32]
AC	VPSA	15	95.3	74.4	0.035	723.6	Sim.	[47]
13X	PSA	10.5	99	80	–	2300–2800	Exp.	[48]
5A	TSA	10	> 94	75–85	0.052	6120–6460	Exp.	[49]
5A	PTSA	10	95.2	94.8	0.069	3800	Sim.	[50]
Mg-MOF-74	TSA	15	97.36	86.5	0.279	1921.3	Sim.	This work

These operating conditions resulted in key performance indices of CO_2 purity, recovery, productivity and power consumption by about 96.22%, 86.5%, 0.279 kg of CO_2 per hour per kg of Mg-MOF-74 and 663.8 kWh per ton of CO_2, respectively.

Acknowledgements

The support received from King Abdulaziz City for Science and Technology (KACST), Carbon Capture and Sequestration Technology Innovation Center (CCS-TIC #32-753) under Project CCS10 and the support of the Deanship of Research (DSR) at KFUPM, Saudi Arabia; are both highly acknowledged.

Appendix A. Supplementary material

Supplementary data associated with this article can be found, in the online version, at http://dx.doi.org/10.1016/j.enconman.2017.11.010.

References

[1] Lee S-Y, Park S-J. A review on solid adsorbents for carbon dioxide capture. J Ind Eng Chem 2015;23:1–11.
[2] Guardian. Antarctic-ship-stranding-delights-climate-change-sceptics. 2014; Available from: www.theguardian.com.
[3] D'Alessandro DM, McDonald T. Toward carbon dioxide capture using nanoporous materials. Pure Appl Chem 2010;83(1).
[4] IPCC. In: Davidson O, Metz B, Coninct H, Loos M, Meyer L, editor. Special report on carbon dioxide capture and storage; 2005.
[5] Ben-Mansour R, Habib MA, Bamidele OE, Basha M, Qasem NAA, Peedikakkal A, et al. Carbon capture by physical adsorption: materials, experimental investigations and numerical modeling and simulations – a review. Appl Energy 2016;161:225–55.
[6] Tan Y, Nookuea W, Li H, Thorin E, Yan J. Property impacts on carbon capture and storage (CCS) processes: a review. Energy Convers Manage 2016;118:204–22.
[7] Songolzadeh M, Ravanchi MT, Soleimani M. Carbon dioxide capture and storage: a general review on adsorbents. World Acad Sci, Eng Technol 2012;70:225–32.
[8] Choi S, Drese JH, Jones CW. Adsorbent materials for carbon dioxide capture from large anthropogenic point sources. Chemsuschem 2009;2(9):796–854.
[9] Siriwardane RV, Shen M-S, Fisher EP, Poston JA. Adsorption of CO_2 on molecular sieves and activated carbon. Energy Fuels 2001;15(2):279–84.
[10] Mazumder S, van Hemert P, Busch A, Wolf KHAA, Tejera-Cuesta P. Flue gas and pure CO_2 sorption properties of coal: a comparative study. Int J Coal Geol 2006;67(4):267–79.
[11] Plaza MG, González AS, Pevida C, Pis JJ, Rubiera F. Valorisation of spent coffee grounds as CO_2 adsorbents for postcombustion capture applications. Appl Energy 2012;99:272–9.
[12] Li Y, Sun R. Studies on adsorption of carbon dioxide on alkaline paper mill waste using cyclic process. Energy Convers Manage 2014;82:46–53.
[13] Spallina V, Pandolfo D, Battistella A, Romano MC, Van Sint Annaland M, Gallucci F. Techno-economic assessment of membrane assisted fluidized bed reactors for pure H_2 production with CO_2 capture. Energy Convers Manage 2016;120:257–73.
[14] Wu W, Kuo P-C. Conceptual designs of hydrogen production, purification, compression and carbon dioxide capture. Energy Convers Manage 2015;103:73–81.
[15] Li J-R, Sculley J, Zhou H-C. Metal-organic frameworks for separations. Chem Rev 2012;112(2):869–932.
[16] Adhikari AK, Lin K-S. Improving CO_2 adsorption capacities and CO_2/N_2 separation efficiencies of MOF-74(Ni, Co) by doping palladium-containing activated carbon. Chem Eng J 2016;284:1348–60.
[17] Yang D-A, Cho H-Y, Kim J, Yang S-T, Ahn W-S. CO_2 capture and conversion using Mg-MOF-74 prepared by a sonochemical method. Energy Environ Sci 2012;5(4):6465–73.
[18] Biswas P, Agrawal S, Sinha S. Modeling and simulation for pressure swing adsorption system for hydrogen purification. Chem Biochem Eng Q 2010;24(4):409–14.
[19] Casas N, Schell J, Pini R, Mazzotti M. Fixed bed adsorption of CO_2/H_2 mixtures on activated carbon: experiments and modeling. Adsorption 2012;18(2):143–61.
[20] Cavenati S, Grande CA, Rodrigues AE. Separation of mixtures by layered pressure swing adsorption for upgrade of natural gas. Chem Eng Sci 2006;61(12):3893–906.
[21] Chaffee AL, Knowles GP, Liang Z, Zhang J, Xiao P, Webley PA. CO_2 capture by adsorption: materials and process development. Int J Greenhouse Gas Control 2007;1(1):11–8.
[22] Cho S-H, Park J-H, Beum H-T, Han S-S, Kim J-N, A 2-stage PSA process for the recovery of CO_2 from flue gas and its power consumption*. In: Carbon dioxide utilization for global sustainability, Proceedings of 7th the International Conference on Carbon Dioxide Utilization, Elsevier BV; 2004. p. 405–410.
[23] Choi W-K, Kwon T-I, Yeo Y-K, Lee H, Song HK, Na B-K. Optimal operation of the pressure swing adsorption (PSA) process for CO_2 recovery. Korean J Chem Eng 2003;20(4):617–23.
[24] Dantas TL, Amorim SM, Luna FMT, Silva Jr IJ, de Azevedo DC, Rodrigues AE, et al. Adsorption of carbon dioxide onto activated carbon and nitrogen-enriched activated carbon: surface changes, equilibrium, and modeling of fixed-bed adsorption. Sep Sci Technol 2009;45(1):73–84.
[25] Dantas TLP, Luna FMT, Silva IJ, de Azevedo DCS, Grande CA, Rodrigues AE, et al. Carbon dioxide–nitrogen separation through adsorption on activated carbon in a fixed bed. Chem Eng J 2011;169(1–3):11–9.
[26] Dantas TLP, Luna FMT, Silva IJ, Torres AEB, de Azevedo DCS, Rodrigues AE, et al. Carbon dioxide–nitrogen separation through pressure swing adsorption. Chem Eng J 2011;172(2–3):698–704.
[27] Gomes VG, Yee KWK. Pressure swing adsorption for carbon dioxide sequestration from exhaust gases. Sep Purif Technol 2002;28(2):161–71.
[28] Krishnamurthy S, Rao VR, Guntuka S, Sharratt P, Haghpanah R, Rajendran A, et al. CO_2 capture from dry flue gas by vacuum swing adsorption: a pilot plant study. AIChE J 2014;60(5):1830–42.
[29] Lee C-H, Yang J, Ahn H. Effects of carbon-to-zeolite ratio on layered bed H2 PSA for coke oven gas. AIChE J 1999;45(3):535–45.
[30] Park J-H, Kim J-N, Cho S-H. Performance analysis of four-bed H2 PSA process using layered beds. AIChE J 2000;46(4):790–802.
[31] Wang L, Liu Z, Li P, Yu J, Rodrigues AE. Experimental and modeling investigation on post-combustion carbon dioxide capture using zeolite 13X-APG by hybrid VTSA process. Chem Eng J 2012;197:151–61.
[32] Wang L, Yang Y, Shen W, Kong X, Li P, Yu J, et al. Experimental evaluation of adsorption technology for CO_2 capture from flue gas in an existing coal-fired power plant. Chem Eng Sci 2013;101:615–9.
[33] Zhang J, Webley PA, Xiao P. Effect of process parameters on power requirements of vacuum swing adsorption technology for CO_2 capture from flue gas. Energy Convers Manage 2008;49(2):346–56.
[34] Ishibashi M, Ota H, Akutsu N, Umeda S, Tajika M, Izumi J, et al. Technology for removing carbon dioxide from power plant flue gas by the physical adsorption method. Energy Convers Manage 1996;37(6):929–33.
[35] Harlick PJE, Sayari A. Applications of pore-expanded mesoporous silicas. 3. Triamine silane grafting for enhanced CO_2 adsorption. Ind Eng Chem Res 2006;45(9):3248–55.
[36] Maurin G, Llewellyn PL, Bell RG. Adsorption mechanism of carbon dioxide in faujasites: grand canonical monte carlo simulations and microcalorimetry measurements. J Phys Chem B 2005;109(33):16084–91.
[37] Akhtar F, Andersson L, Keshavarzi N, Bergström L. Colloidal processing and CO_2 capture performance of sacrificially templated zeolite monoliths. Appl Energy 2012;97:289–96.
[38] Cheung O, Bacsik Z, Liu Q, Mace A, Hedin N. Adsorption kinetics for CO_2 on highly selective zeolites NaKA and nano-NaKA. Appl Energy 2013;112:1326–36.
[39] Ansys-Fluent; 2016; Available from: http://www.ansys.com.
[40] He W, Lv W, Dickerson JH, Gas diffusion mechanisms and models. In: Gas transport in solid oxide fuel cells. Cham: Springer International Publishing; 2014. p. 9–17.
[41] Incropera; Frank PD, David P. Fundamentals of heat and mass transfer. J. Wiley; 2007.
[42] Dantas TLP, Luna FMT, Silva Jr IJ, Torres AEB, de Azevedo DCS, Rodrigues AE, et al. Modeling of the fixed – bed adsorption of carbon dioxide and a carbon dioxide – nitrogen mixture on zeolite 13X. Braz J Chem Eng 2011;28(3):533–44.
[43] Funazukuri T, Kong C, Kagei S. Effective axial dispersion coefficients in packed beds under supercritical conditions. J Supercrit Fluids 1998;13(1–3):169–75.
[44] Mason JA, Sumida K, Herm ZR, Krishna R, Long JR. Evaluating metal–organic frameworks for post-combustion carbon dioxide capture via temperature swing adsorption. Energy Environ Sci 2011;4(8):3030.
[45] Qasem NAA, El-Shaarawi MAI. Improving ice productivity and performance for an activated carbon/methanol solar adsorption ice-maker. Solar Energy (2013); 98 (Part C):523–542.
[46] Qasem NAA, El-Shaarawi MAI. Thermal analysis and modeling study of an activated carbon solar adsorption icemaker: Dhahran case study. Energy Convers Manage

2015;100:310–23.
[47] Shen C, Liu Z, Li P, Yu J. Two-stage VPSA process for CO_2 capture from flue gas using activated carbon beads. Ind Eng Chem Res 2012;51(13):5011–21.
[48] Cho SH, Park JH, Beum HT, Han SS, Kim JN. A 2-stage PSA process for the recovery of CO2 from flue gas and its power consumption, Stud Surf Sci Catal 2004:405–410.
[49] Merel J, Clausse M, Meunier F. Experimental investigation on CO_2 post − combustion capture by indirect thermal swing adsorption using 13X and 5A zeolites. Ind Eng Chem Res 2008;47(1):209–15.
[50] Mendes PAP, Ribeiro AM, Gleichmann K, Ferreira AFP, Rodrigues AE. Separation of CO_2/N_2 on binderless 5A zeolite. J CO_2 Utili 2017; 20: 224–233.